Controlled Anisotropic Growth of Hydroxyapatite by Additive-Free Hydrothermal Synthesis

Jordi Sans,[1,2] Vanesa Sanz,[3] Jordi Puiggalí,[1,2,4] Pau Turon,[3,*] and Carlos Alemán[1,2,4*]

[1] Departament d'Enginyeria Química, EEBE, Universitat Politècnica de Catalunya, C/ Eduard Maristany, 10-14, Ed. I2, 08019, Barcelona, Spain

[2] Barcelona Research Center in Multiscale Science and Engineering, Universitat Politècnica de Catalunya, C/ Eduard Maristany, 10-14, 08019, Barcelona, Spain

[3] B. Braun Surgical, S.A. Carretera de Terrasa 121, 08191 Rubí (Barcelona), Spain

[4] Institute for Bioengineering of Catalonia (IBEC), The Barcelona Institute of Science and Technology, Baldiri Reixac 10-12, 08028 Barcelona Spain

[*] Correspondence to: pau.turon@upc.edu and carlos.aleman@upc.edu

1

ABSTRACT

The synthesis of hydroxyapatite (HAp) with different shapes and sizes has attracted increasing attention because the applicability of this ceramic material depends on structure-properties relationships (*i.e.* the dimensions and morphology of HAp crystals determine properties such as the bioactivity and mechanical strength). Although different synthetic routes based on the addition of surfactants, organic modifiers or dispersants have been proposed to control the growth of HAp crystals, many efforts are being devoted to simplify the whole process using simple parameters such as pH. However, the control of the morphology is still poor and shows low reproducibility. In this work, a new additive-free synthetic route, which is based on the hydrothermal method and the utilization of non-aqueous solvents, is proposed. The influence of the synthesis parameters such as pH, concentration of starting solutions and the solvent on relevant features such as phase purity, crystallinity, crystallite size and morphology has been examined using spectroscopic techniques, X-ray diffraction and scanning electron microscopy. As a consequence, this work presents an easy and robust method based only in the use of organic solvent and the control of the pH that produces pure and crystalline HAp with controlled shape and size. This method has been used to elucidate some of the key aspects of the crystal growth mechanism and to synthesize HAp crystals with different and well-defined shapes (*e.g.* belts, rods, flakes needle-like or polymorph) and size, in a reproducible way.

INTRODUCTION

In the last decades, synthetic hydroxyapatite (HAp) has gained a lot of interest, especially in the biomedical field.[1-6] Although HAp structure and its outstanding biocompatibility have been extensively studied,[7,8] new synthetic methodologies to control particle's shape and size have been recently developed to fulfill the requirements of biomedical and industrial applications based on this ceramic material.[9–12] Thus, properties such as mechanical strength, bioactivity or adsorption capability are directly rooted in the morphology of the HAp nanocrystals.[13] Indeed, the surface activity of HAp increases drastically when the grain size is less than 100 nm,[14,15] and such an effect can be used to promote bone regeneration and bone replacement because it mimics the morphology of the mineral found in hard tissues existing in physiological environments.[16] Moreover, surface charge also depends on the exposed crystalline planes and, consequently, on the shape of the HAp nanoparticles, as was shown by measuring the adsorption of DNA onto different HAp surfaces.[17]

There are several techniques for the synthesis of HAp, which are mainly focused on controlling its shape, although other parameters like polydispersity, crystallinity or phase purity are also significantly affected by the preparation procedure. The most common synthetic techniques are chemical precipitation (CP),[18] sol–gel,[19] hydrothermal (HT),[20] and solid state.[21] HT synthesis of HAp is one of the most reported techniques, only surpassed by the CP method, which is the simplest technique and the one with lowest economic cost.[22] HAp particles prepared using the HT method exhibit much higher crystallinity and phase purity than those obtained using the CP route.[5] In fact, the HT method can be considered as a CP in which the crystal growth is conducted under pressure and temperature during the aging step.

The most important disadvantage of the HT synthesis is the poor control on the morphology and size distribution of the nanoparticles.[6,23,24] Significant efforts have been made to understand the HAp crystal growth mechanism by studying, among others, the effect of the pH, Ca/P ratio, ageing time and temperature.[25-27] In general, it was observed that a high pH promoted a isotropic growth, whereas an acid pH led to an anisotropic growth[28] (*i.e.* 1D nanorods or 2D nanoplates) and reduced the phase purity.[27] Nevertheless, some discrepancies appear in the literature as the synthesis of nanorods under alkaline and neutral conditions is also described.[29,30] These disparities can be attributed to thermo-kinetic effects since in those studies the hydrothermal treatment was applied using different stirring velocities, temperatures and ageing times.

On the other hand, the addition of organic modifiers, non-ionic surfactants or dispersants, as for example ethylenediaminetetraacetic acid (EDTA), polyethylene glycol (PEG) or ethanolamine, respectively, have been successfully used as templates for anisotropic growth of HAp crystals at mild HT conditions.[31-35] In all cases, mechanisms based on the balance of ions in the solutions (*e.g.* the concentration of free Ca^{2+} in the solution decreases by chelation with EDTA, affecting the HAp nucleation[32]) and the absorption of OH^- groups on the growing faces of the first clusters[36] were proposed. Recently, the same mechanism was extrapolated to a synthetic route without any surfactant,[37] even though the anisotropic growth of the achieved HAp morphologies was still far from those obtained using the aforementioned surfactants and organic modifiers. That fact might be associated to the correlation between the OH^- groups and Ca^{2+} free ions when adjusting the pH conditions of the solution, whereas such species kept uncorrelated when surfactants were used as templates.

In this work, we develop a HT route without using any additive (surfactant, organic modifier or dispersant) for the synthesis of highly crystalline HAp, which is

independent of the presence of OH⁻ groups and free Ca^{2+} ions. More specifically, the production of flakes, rods, and belts with different sizes has been regulated by controlling the solvent, pH and concentration of one of the starting solutions. The growing mechanism is discussed by analyzing the chemical species, phase purity, crystallinity, crystallite size and morphology of samples synthesized using different experimental conditions.

EXPERIMENTAL METHODS

Detailed description of the materials and the applied characterization techniques, FTIR and Raman spectroscopy, wide angle X-ray scattering (WAXS) and scanning electron microscopy (SEM) is provided in the ESI.

Synthesis of HAp

HAp samples were synthesized using as starting materials $(NH_4)_2HPO_4$ and $Ca(NO_3)_2$ solutions with concentrations ranging from 100 to 750 mM (*i.e.* the concentrations of the both solutions were identical in all studied cases to get a stoichiometric Ca/P ratio of 1.67). Calcium nitrate was dissolved in the organic solvent with no water. The pH, which varied from 5.7 to 11, was adjusted with ammonium hydroxide 30% w/w aqueous solutions and measured using a Crison GPL 21 pH meter. On the other hand, the pH of the $(NH_4)_2HPO_4$ solutions, which were prepared using de-ionized water in all cases, was not adjusted.

15 mL of $(NH_4)_2HPO_4$ solution were added drop-wise (2 mL/min) to 25 mL of $Ca(NO_3)_2$ solution and left aging for 1 h. All the process was performed under gentle agitation (150 rpm). The mixture was immediately transferred to an autoclave Digestec DAB-2 where the HT method was applied for 24 h at 150 ºC. The autoclave was

allowed to cool down before opening. A white precipitate was obtained, separated and washed sequentially at 8000 rpm for 5 min with water and a 60/40 v/v ethanol/water mixture (twice). Freeze-drying was applied for 3 days to minimize the shrinkage and morphological deformation of the obtained particles.[36,38] At the end of the whole process, a white powder was obtained.

RESULTS AND DISCUSSION

The present discussion relies on the fact that the dependence of the Ca^{2+}, PO_4^{3-} and $(HPO_4)^{2-}$ ions on the OH^- specie is no longer maintained when the pH of a non-aqueous solution is changed. Previous studies indicated that the concentration of the starting solutions affects the crystal growth,[36] whereas the variation of the OH^- concentration by changing the pH promotes the precipitation of HAp but decreases its anisotropy.[37] However, the literature reports conflicting results since controlling ions balance by adjusting the pH of mixtures of aqueous solutions is a complex task, as changing the pH increases the solubility (*i.e.* the super-saturation value) but the amount of OH^- ions as well. Our approach is based on the fact that a better control of the ions balance is expected by separating the amount of free Ca^{2+} ions from the amount of OH^- ions by adjusting the pH of the $Ca(NO_3)_2$ non-aqueous solution only. This is anticipated to improve the control of the crystal growth.

Table 1 lists and labels, as sample s#, all the conditions used in this study to prepare HAp. In the next sub-section, the effects of the solvent on the chemical composition, phase purity, crystallinity and crystallize size are investigated using FTIR, Raman spectroscopy and WAXS. After this, the influence of changing the pH and the concentration of the starting solution on the crystal growth has been examined. Finally,

the morphology of the prepared samples, as determined by SEM, has been discussed in a separate sub-section.

Table 1. Experimental conditions used to obtain the HAp samples studied in this work. Samples, which are identified with the label s# (ranging from s1 to s15) were prepared by the HT method using $(NH_4)_2HPO_4$ and $Ca(NO_3)_2$ solutions as starting materials. *Concentration* refers to the concentration of the starting $Ca(NO_3)_2$ and $(NH_4)_2HPO_4$ solutions. *Solvent r*efers to the solvent used to prepare the $Ca(NO_3)_2$ solution since $(NH_4)_2HPO_4$ solutions were prepared using de-ionized water in all cases. *pH* refers to the pH of the $Ca(NO_3)_2$ solution, which was adjusted using ammonium hydroxide (the pH of the $(NH_4)_2HPO_4$ solutions was kept around 7.9 in all cases).

Sample	*Concentration* (mM)	*Solvent*	*pH*
s1	100	Water	10.5
s2	100	Methanol	10.5
s3	100	Ethanol	10.5
s4	100	Isopropanol	10.5
s5	100	Ethanol	10
s6	100	Ethanol	11
s7	500	Ethanol	10
s8	500	Ethanol	11
s9	750	Ethanol	10
s10	750	Ethanol	11
s11	500	Ethanol	10.5
s12	100	Ethanol	11.5
s13	500	Ethanol	11.5
s14	500	Ethanol	5.7
s15	500	Ethanol	9.9

Effects of the solvent

Figure S1 shows the FTIR spectra of samples synthetized using 100 mM $Ca(NO_3)_2$ solutions in water (s1), methanol (s2), ethanol (s3) and isopropanol (s4) at pH 10.5.

Methanol exhibits a dielectric constant (ε) that is less than a half that of water (32.7 vs 80.1) and a loss of hydrogen bonding capacity (*i.e.* methanol is more volatile than water). The polarity decreases with increasing size of the alcohol (*i.e.* ε= 24.5 and 17.9 for ethanol and isopropanol, respectively), the vapor pressure following the same tendency (*i.e.* methanol is more volatile than ethanol, that in turn is more volatile than isopropanol). As shown, the spectra are dominated by the PO_4^{3-} vibrational modes in all cases. A detailed analysis of the 850 to 1150 cm^{-1} region (Figure 1) evidences a slight blueshift (< 5 cm^{-1}) with decreasing solvent polarity for the P–O non-degenerated symmetric stretching mode at ν_1= 957 cm^{-1} and a clear redshift (~7 cm^{-1}) for the P–O triply degenerated asymmetric stretching mode at ν_{3c}= 1016, respectively (*i.e.* ν_{3a} and ν_{3b} remain at 1084 and 1062 cm^{-1} with a maximum variation of 2 and 1 cm^{-1}, respectively, independently of the solvent).[17] These shifts have been attributed to the presence of HPO_4^{2-} groups, which cause crystal imperfections in the HAp lattice. Thus, the charge balance modifications of the existing PO_4^{3-} tetrahedra and/or the existence of new apatitic phases containing explicitly HPO_4^{2-} groups, due to the excess of crystalline distortions, lead to the generation of non-stoichiometric HAp.[39] The presence of HPO_4^{2-} is consistent with ^{31}P NMR analyses reported for HAp prepared using a $Ca(NO_3)_2$ solution in ethanol and a similar synthetic route.[40]

During the synthesis process, CO_2 adsorbed from the atmosphere can replace in form of CO_3^{2-} both OH^- (type-A, the channel location) and PO_4^{3-} (type-B, tetrahedral location) ions of the crystal lattice. This substitution process has been extensively studied, as it introduces crystal imperfections that are believed to affect the morphology of the final crystals.[17,39] However, CO_2 is less soluble in organic solvent than in water.[41,42] Interestingly, the absence of peaks in the region from 1400 to 1600 cm^{-1} (Figure 1) reflects the lack of carbonate ions in the crystal lattice of samples s1-s4. This

observation has been attributed to: 1) the existence of HPO_4^{2-} ions in the same substituting sites of the crystal lattice; and 2) adjusting only the pH in the $Ca(NO_3)_2$ solution, leads to less basic mixed final solution that reduces the diffusion and solubility of CO_2.
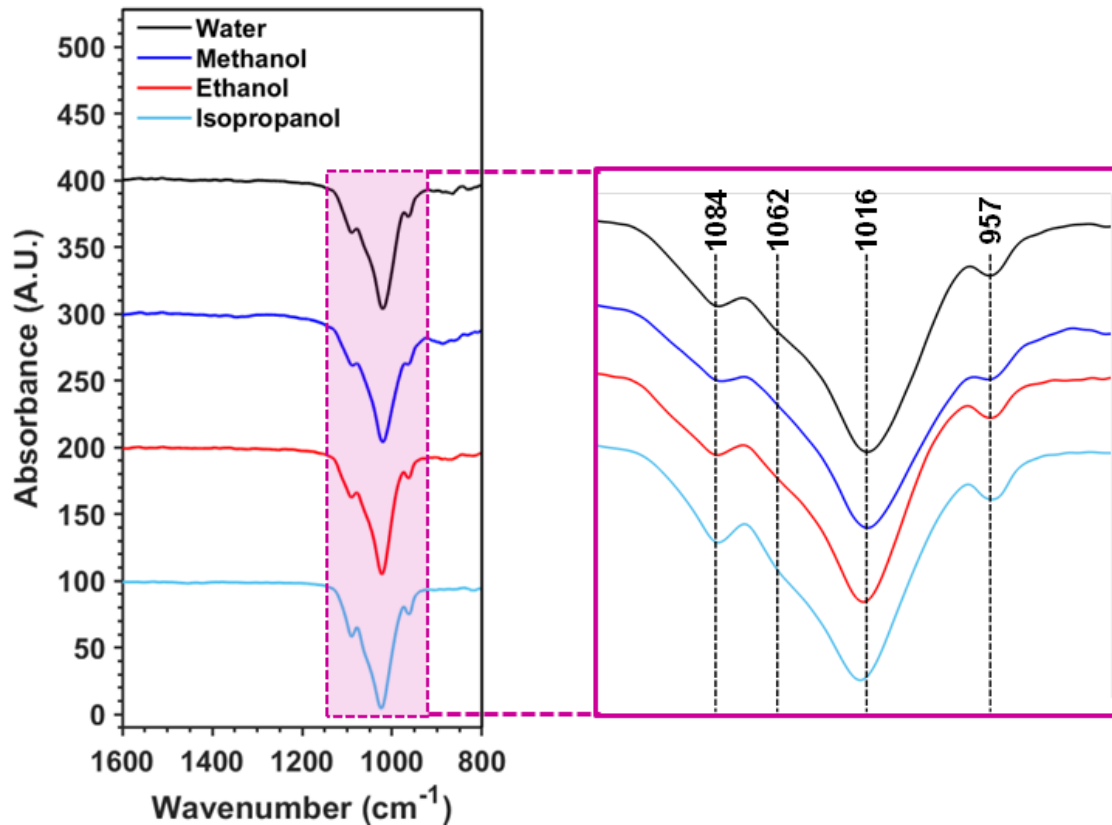

Figure 1. FTIR spectra (800-1600 cm^{-1}) of samples prepared using 100 mM $Ca(NO_3)_2$ solutions with different solvents at pH 10.5 (s1-s4 in Table 1).

Phase purity in HAp prepared by CP and HT is known to be highly dependent on the pH conditions, stoichiometry and other thermo-kinetic parameters, such as the aging time.[43] However, the solvent can also affect the purity, promoting the formation of other crystalline phases, such as β-tricalcium phosphate (β-TCP) and amorphous calcium phosphate (ACP). Although WAXS is commonly used for phase identification, complete characterization of apatitic materials is sometimes difficult. Raman spectroscopy represents an excellent alternative to determine different apatite crystalline

phases, as was recently shown.[44] Raman spectra of s1-s4 samples (Figure 2) are dominated by the four characteristic regions of HAp vibrational modes, which correspond to the following PO_4^{3-} internal modes: ν_1= 962 cm^{-1} (P–O symmetric stretching); ν_2= 400-490 cm^{-1} (doubly degenerated O–P–O bending); ν_3= 570-625 cm^{-1} (P–O triply degenerated asymmetric stretching); and ν_4= 1020-1095 cm^{-1} (triply degenerated O–P–O bending mode).[45,46] Interestingly, s2 (methanol) is the only sample presenting a splitting of the main ν_1 mode in form of two peaks located at 983 cm^{-1} and 900 cm^{-1}, which has been attributed to the presence of dicalcium phosphate dehydrate (DCPD)[39] and ACP.[44] Accordingly, other DCPD peak and shoulder can be found at 392 cm^{-1} and 417 cm^{-1} respectively. Hence, the fact that s1 does not present new apatitic phase suggests that the shift obtained in the FTIR spectrum is attributed to the generation of – $[PO_4]^{2-}$ tetrahedra in the crystalline sites of PO_4^{3-}, which is in agreement with the difference in the dielectric constant and hydrogen bonding capacity between methanol and water. Thus, water favors the formation of HPO_4^{2-} by capturing the proton of HPO_4^{2-} group. Consistently, the crystallinity, as measured by XRD (see below), is lower for s1 than for s2 due to the imperfections introduced in the crystal lattice.

Semi-quantitative analysis regarding the relative phase distributions (% content of each phase) was determined using the intensity of the 900, 962 and 983 cm^{-1} bands, which correspond to the ACP, HAp and DCPD phases, respectively, and applying Eqs 1-3:[44]

$$\% \text{ ACP} = \frac{I_{900}}{I_{900}+I_{962}+I_{983}} \times 100 \qquad (1)$$

$$\% \text{ HAp} = \frac{I_{962}}{I_{900}+I_{962}+I_{983}} \times 100 \qquad (2)$$

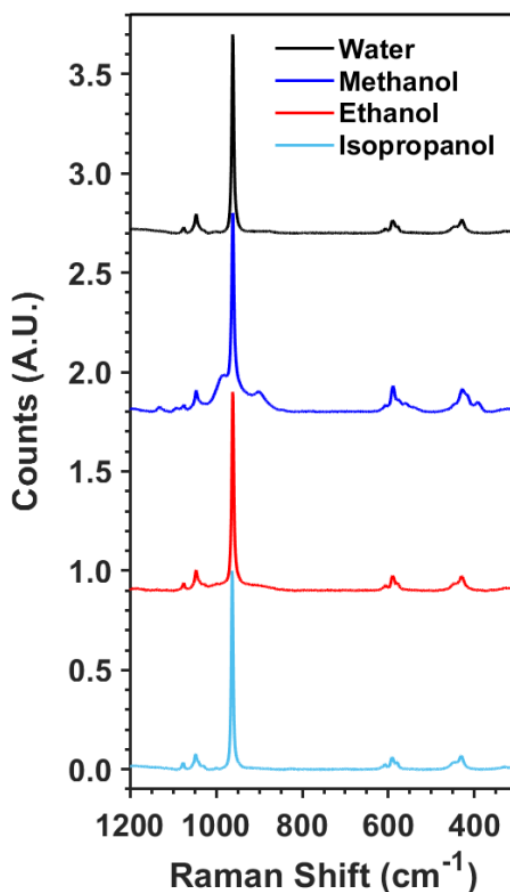$$\% \text{ DCPD} = \frac{I_{983}}{I_{900}+I_{962}+I_{983}} \times 100 \qquad (3)$$

Figure 2. Raman spectra (300-1200 cm^{-1}) of the samples prepared using 100 mM $Ca(NO_3)_2$ solutions with different solvents at pH 10.5 (s1-s4 in Table 1).

For s2, the content of ACP, HAp and DCPD was 7.8 %, 78.1 % and 14.1 %, respectively. Splitting of the main v_1 peak appears when other apatite phases introduce distortions and defects on the four PO_4^{3-} equivalent tetrahedra of HAp. This distortion can also be observed by measuring the full width at half maximum (FWHM) of the v_1 mode, being 5.7 cm^{-1} for s2. This value decreases to 4.5 cm^{-1} for s1 and s3, and to 3.3 cm^{-1} for s4, reflecting a higher degree of order and crystallinity. These FWHM values are consistent with HAp purity, which is only reduced to 78.1% for samples prepared using a $Ca(NO_3)_2$ methanol solution. The apparition of ACP and DCPD phases in s2 has been attributed to the reduced availability of OH^- ions during the nucleation and growing steps since the dissociation constant is higher for methanol than for ethanol and

isopropanol (*i.e.* the pKa decreases as follows: 15.3 (methanol) < 15.9 (ethanol) < 17.1 (isopropanol). Consistently, the intensity of the peak at 3573 cm^{-1} (Figure S2), which is associated to the O–H stretching mode, decreases from 0.23 for s4 (isopropanol) to 0.21 for s1 (water) and s3 (ethanol), and to 0.18 for s2 (methanol).

In summary, the utilization of organic solvents reduces the availability of OH$^-$ ions with respect to typically used basic aqueous solutions, favoring the anisotropic growth of HAp. More specifically, FTIR and Raman spectroscopy studies on s1-s4 evidence that: 1) the lack of OH$^-$ ions in the charge balance of the solutions leads to more defects during the nucleation and growing steps; 2) HPO$_4^{2-}$ occupies the hydroxyl or PO$_4^{3-}$ sites of the crystal lattice introducing defects and distortion; 3) for the synthesis of highly crystalline HAp, the amount of available OH$^-$ at a given pH can be controlled using solvents with different pKa; and 4) the excess of distortion might cause the creation of other apatitic phases.

Quantitative measurements about the crystalline growth can be obtained using WAXS. Without thermal treatment, HAp crystallizes in a hexagonal structure (P6$_3$/m space group).[47] WAXS spectra recorded for s1-s4, which are displayed in Figure 3a, are consistent with Raman observations. All samples display the characteristic diffractions peaks at 2θ= 25.9º, 28.9º, 31.7º, 32.1º, 32.8º 34.0º and 39.8º, corresponding to the (002), (210), (211), (112), (300), (202) and (310) reflections, respectively (JCPDS card number 9-0432). The sharp peak at 2θ= 30.1º for s2 has been attributed to the already discussed apparition of the DCPD phase (JCPDS card number 9-0077) when a Ca(NO$_3$)$_2$ methanol solution is used as starting material. On the other hand, although the 2θ= 30.1º peak can be also observed in the spectrum recorded for s3, the ratio in intensities leads to a HAp content higher than 95%, which has been considered as high purity HAp crystal.
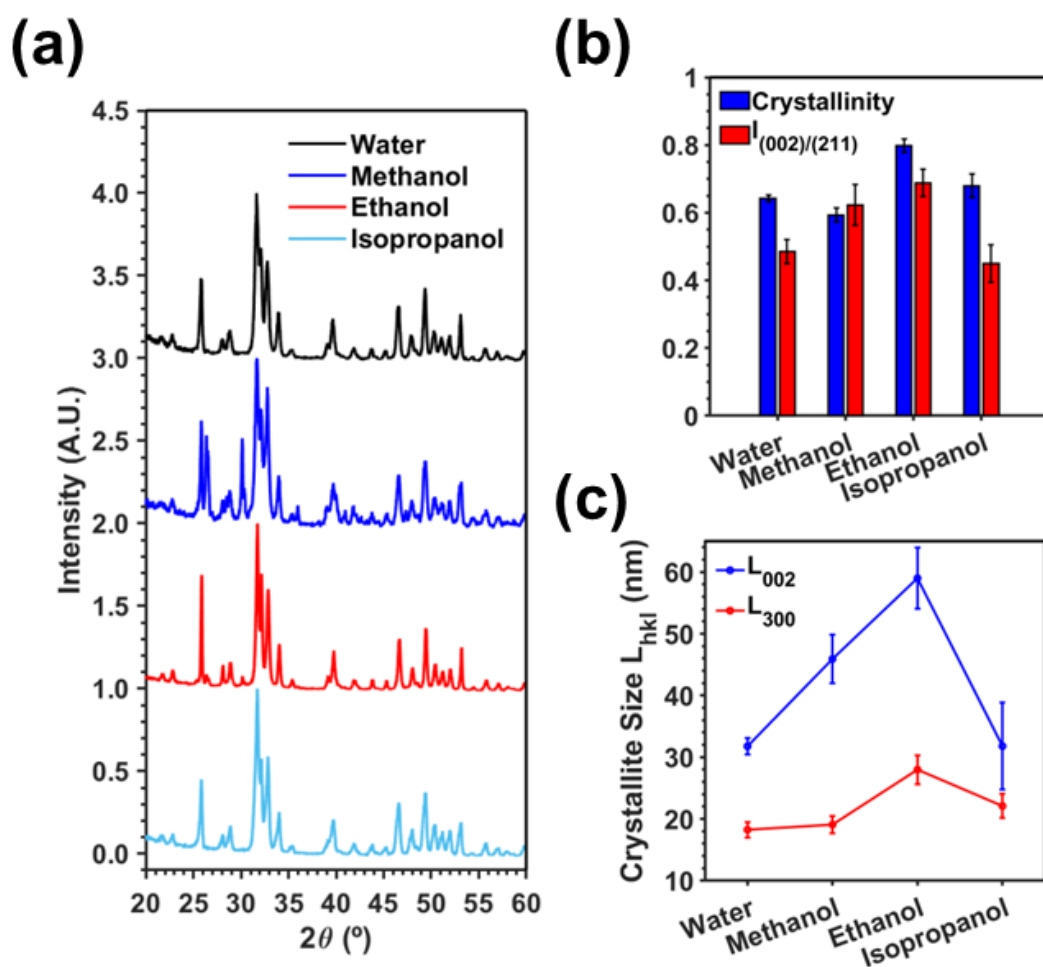
Figure 3. WAXS results of samples prepared using 100 mM $Ca(NO_3)_2$ solutions with different solvents at pH 10.5 (s1-s4 in Table 1): (a) WAXS patterns in the characteristic 2θ range of HAp, from 20º to 60º; (b) Comparison of crystallinity and $I_{002/211}$ ratio; and (c) Crystallite size in the direction perpendicular to the (002) and (300) planes, L_{002} and L_{300}, respectively.

The anisotropic growth of the HAp crystals has been characterized analyzing the (002) plane, which corresponds to the *c*-axis direction of the unit cell and, thus, the length of elongated HAp particles.[27,48] Figure 3b compares the intensity ratio of the (002) plane with the regular and characteristic (211), referred as $I_{(002)/(211)}$, for s1-s4. As is shown, for the same pH, the acidic nature of each solvent regulates the growth along the *c*-axis. Samples prepared using the solvent with the highest pKa, isopropanol (s4), show the smallest growth along the *c*-axis with a ratio of 0.45 only. However, $I_{(002)/(211)}$

increases with decreasing solvent's pKa, a value of 0.69 being obtained for the samples derived from ethanol solutions (s3). Apparently, this tendency is broken for samples prepared with methanol (s2), which exhibit a ratio of 0.62. However, consideration of the crystallinity for the HAp phase (χ_c), which was determined as described in the Supporting Information (Eq. S1), provides understanding of such behavior. Figure 3b shows that the χ_c for s2 (0.60) is smaller than for s3 (0.80) and s4 (0.68), suggesting that the reduction of the OH^- concentration affects the general growth of the crystal. Finally, the higher amount of OH^- in alkaline water, as compared with the alcohol ones, reduces the growth in the c-axis ($I_{(002)/(211)}$= 0.49) despite presenting χ_c= 0.64.

The crystallite size in the direction perpendicular to the (002) and (300) planes (L_{002} and L_{300}, respectively) was estimated using the Debye-Scherrer equation (Eq. S2) to evaluate the anisotropic growth in the c-axis. Figure 3c, which compares the values obtained for s1-s4, shows that L_{002} ranges from 30 to 60 nm while L_{300} is more homogenous varying from 18 to 28 nm. These values reveal elongated crystallite shapes, independently of the solvent. This has been attributed to the fact that, despite the adjustment of the pH at 10.5 of the $Ca(NO_3)_2$ solution, the pH of the mixture obtained after the addition of the $(NH_4)_2HPO_4$ solution is not alkaline. Although the size of the crystallites is significantly higher for s3 (ethanol) than for s2 (methanol), which is consistent with their χ_c values (Figure 3b), the L_{002}/L_{300} ratio remains constant, evidencing that the stoichiometry and balance of ions during the synthesis is the optimum.

Effects of the concentration and the pH

Derived from the results of last section, ethanol was chosen as the solvent for $Ca(NO_3)_2$. Spectroscopic and diffraction studies were conducted on HAp samples

obtained using different concentrations (100, 500 and 750 mM) and pH (10 and 11), which have been labelled as s5-s10 in Table 1.

Figure S3 shows the FTIR and Raman spectra, as well as the WAXS patterns of samples s5-s10. The distribution of apatitic phases, as obtained by Raman spectroscopy (Eq. 1-3), is shown in Table 2, reflecting that, in addition of HAp, some samples (s5, s6 and s9) contain ACP and DCPD. This feature is particularly noticeable for s9, which exhibits 69.6% of HAp only (*i.e.* the HAp content is $\geq$ 90% for s5 and s6), affecting χ_c. Although the χ_c values obtained for the different samples do not follow a defined trend, as is reflected in Figure 4a, important conclusions can be drawn when χ_c is analyzed in combination with apatitic phase distribution. Thus, χ_c decreases when the $Ca(NO_3)_2$ concentration increases from 100 to 500 mM, independently of the pH. For samples obtained from a 750 mM $Ca(NO_3)_2$ solution, the χ_c boosts to 0.74 at pH 10 (s9) and reduces to the lowest value, $\chi_c = 0.64$, at pH 11 (s10), breaking the tendency. In order to interpret these results, the apatitic phase distributions must be taken into account. Distortions in the HAp crystal lattice result in a reduction of χ_c until they are important enough to cause a transition into a different ordered crystalline phase, indirectly increasing the χ_c value since this parameter only considers the HAp phase. Accordingly, samples obtained using a $Ca(NO_3)_2$ concentration of 500 mM (s7 and s8) are the optimum for growing pure HAp, even though they exhibit the lowest χ_c value. Besides, pH 11 favors the crystal growth of pure and ordered HAp, even for s10 if the contribution of the other apatitic phases is neglected.

Analysis of the $I_{(002)/(211)}$ ratio obtained from WAXS profiles (Figure 4b) reflects a drastic and systematic reduction of the anisotropic growth when the pH increases from 10 to 11. This observation is supported in Figure 4c by the ratio between the intensities of the Raman bands at 3573 and 962 cm^{-1}, I_{3573}/I_{962}, which correspond to the O–H

15

stretching mode and the PO_4^{3-} internal modes of HAp, respectively. The reduction of I_{3573}/I_{962} with increasing pH is consistent with a decrease of the amount of OH^- groups in the crystal lattice. These results indicate that the incorporation of the OH^- groups during HAp nucleation and growing does not depend on the pH of the ethanol solution, which favors the anisotropic growth of the HAp crystals. Finally, Figure 4d compares the values of L_{002} and L_{300} for s5-s10. Results show that the HT growing step becomes faster with increasing $Ca(NO_3)_2$ concentration due to the higher availability of free ions, even though that faster growth can cause crystals imperfections and a reduction of the crystallinity.

Table 2. Distribution of apatitic phases in s5-s10 HAp samples as determined by Raman spectroscopy (Eq. 1-3).

Sample	$[Ca(NO_3)_2]$ (mM) / pH	ACP (%)	HAp (%)	DCPD (%)
s5	100 / 10	3.9 ± 0.8	90.0 ± 1.5	6.1 ± 1.4
s6	100 / 11	1.2 ± 0.3	95.2 ± 0.6	3.6 ± 0.5
s7	500 / 10	0.0	100.0	0.0
s8	500 / 11	0.0	100.0	0.0
s9	750 / 10	14.6 ± 1.0	69.6 ± 1.3	15.8 ± 1.2
s10	750 / 11	0.0	100.0	0.0

In order to study more deeply the effect of pH in the growth of HAp crystals, WAXS analyses were compared for samples prepared using 100 and 500 mM $Ca(NO_3)_2$ ethanol solutions at pH 10 (s5 and s7), 10.5 (s3 and s11), 11 (s6 and s8) and 11.5 (s12 and s13). Figure 5 represents the variation of the $I_{(002)/(211)}$ ratio with the pH for the two examined concentrations. It is worth noting that the reduction of the anisotropic growth with increasing pH displayed in Figure 4b is maintained. The largest variation of $I_{(002)/(211)}$ is observed for samples obtained using a 500 mM $Ca(NO_3)_2$ solution, from 0.86 (pH 10.5)

to 0.50 (pH 11.5). Further analyses of samples prepared at pH 5.7 and 9.9 (s14 and s15, respectively) showed a poor presence of HAp phase (Figure S4).
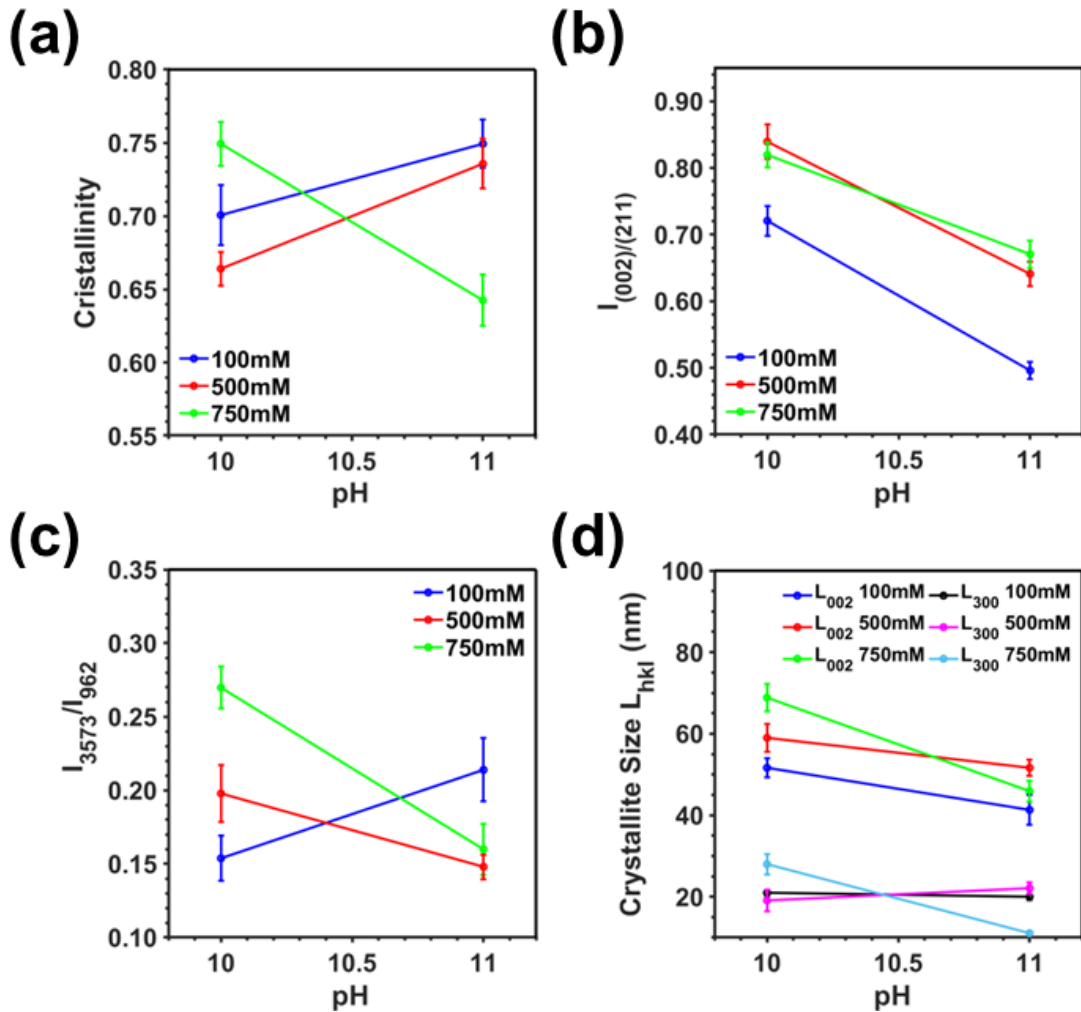

Figure 4. Summary of the results derived from Raman and WAXS studies of samples prepared using $Ca(NO_3)_2$ solutions with different concentrations and pH (s5-s10): (a) Crystallinity and (b) $I_{002/211}$ ratio from WAXS patterns, (c) $I_{3573/962}$ ratio from Raman spectra, and (d) crystallite size of the planes (002) and (300) planes, L_{002} and L_{300}, respectively, WAXS patterns.

The following relevant conclusions can be extracted from results derived for s5-s15 samples: 1) alkaline solutions are desirable for achieving highly crystalline and pure HAp crystals; 2) the concentration of the starting solutions, which is directly related to the amount of free ions in the medium, controls the rate of crystal growth, crystallite

sizes increasing with the concentration; and 3) the anisotropy of the crystals decreases with increasing pH. It should be noted that, although the pH used in this study for the $Ca(NO_3)_2$ solution is alkaline, the pH reached after the addition of the $(NH_4)_2HPO_4$ solution ranges from acid to slightly alkaline (Figure S5), achieving highly directional crystalline growth. Thus, small pH differences in the prepared $Ca(NO_3)_2$ solutions can result in significant pH differences in the final mixtures, inducing important structural changes. The fact that samples prepared in this study present similar or higher levels of HAp crystallinity and purity supports the use of a non-aqueous solvent to adjust the desired pH without drastically increasing the amount of OH^- groups in the final mixed solution. Moreover, this strategy enhances the crystal anisotropy without decreasing the HAp crystallinity and purity.
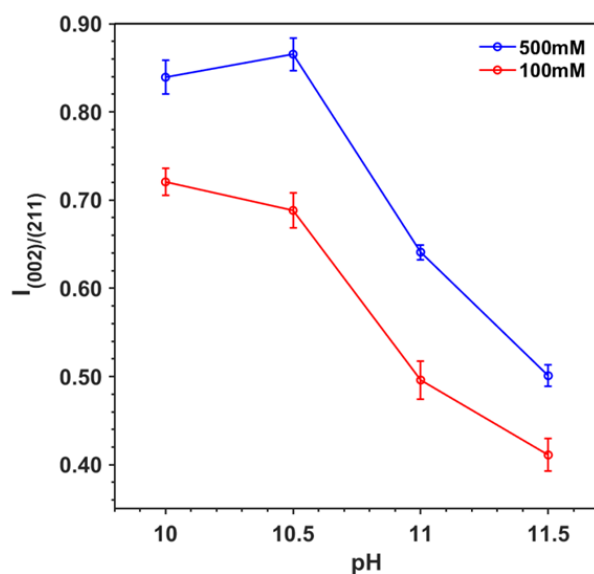

Figure 5. Variation of the $I_{002/211}$ ratio, as determined from WAXS diffractograms, with the pH for samples prepared using 100 and 500 mM $Ca(NO_3)_2$ ethanol solutions.

Morphology

Results from morphological studies using SEM are summarized in Table 3 and Figure 6. Due to the use of non-aqueous solvents, most of the samples show elongated morphologies. Apparently, pH is the most important parameter for controlling the

18

morphology of the crystals. At pH 11.5 polymorph spherical shapes are obtained (Figure 6a), the anisotropy of the growth increases with decreasing pH. Thus, rod shapes and belts are observed at pH 11 (Figure 6b) and pH 10 (Figure 6c), respectively. These morphological differences are huge compared to the already reported research on the effect of the pH,[37] which has been attributed to both the utilization of non-aqueous solvents and to the adjustment of the pH of the calcium source only.

Table 3. Morphology and average size of the HAp structures obtained for samples prepared using different conditions (solvent, concentration of the starting solutions and pH). The size is expressed as diameter (D), length (L) and/or width (W) depending on the morphology.

| Sample	Solvent / concentration / pH	Morphology	Size (nm)
s2	Methanol / 100 mM / 10.5	Needle flake-like	L= 180±43
s5	Ethanol / 100 mM / 10	Belts	W=47±10, L= 361±161
s7	Ethanol / 500 mM / 10	Belts	W= 29±12, L= 854±368
s8	Ethanol / 500 mM / 11	Rods	D= 12±2, L= 41±9
s9	Ethanol / 750 mM / 10	Belts	W= 74±35, L= 1392±573
s10	Ethanol / 750 mM / 11	Rods	D= 34±7, L= 124±24
		Spherical polymorph	D= 46±15
s13	Ethanol / 500 mM / 11.5	Spherical polymorph	D= 31±10
s15	Ethanol / 500 mM / 9.9	Belts	W=98±17, L= 3259±1847
		Rods	D= 1308±584, L= 13161±5048
		Plates	D= 5289±2891
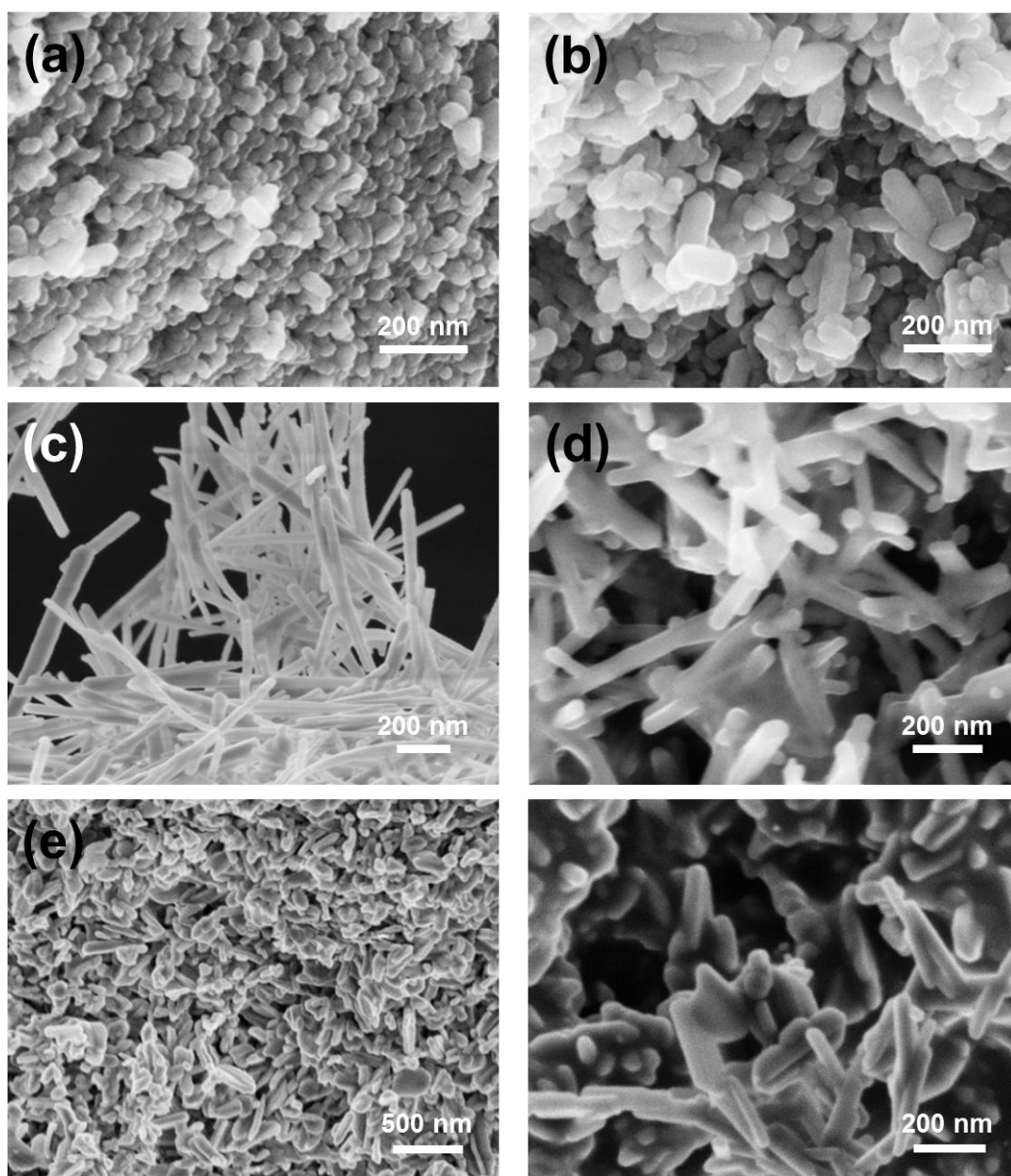
Figure 6. High-magnification SEM micrographs of representative shapes obtained for the following samples: (a) s10 (spherical polymorphs); (b) s8 (rod shapes); (c) s9 (belts); and (d) s5 (belts with smaller aspect ratio). (e) Low- and high-magnification micrographs (left and right, respectively) for s2 samples (needle flake-like geometry).

In general, concentration plays an important role in controlling the size and distribution of the crystals: the length of the crystals increases with the concentration of the starting solution, which has been associated to the higher presence of available ions during the crystalline growth. It is worth mentioning that sample s10 (750 mM, pH 11),

which apparently does not follow this trend, exhibits not only rods but also a population of polymorph spherical shapes that justifies the reduction on the crystallite size compared with the other samples. According to the WAXS analysis discussed above and SEM micrographs (Figure 6d and Table 3), sample s5 (100 mM, pH 10) shows less anisotropy (*i.e.* lower aspect ratio) than s7 (500 mM, pH 10). This confirms the growing process mechanism proposed in the literature,[27,49] which involve two different steps: 1) nucleation and growth of the nuclei; and 2) growth by agglomeration.

Although the use of methanol was discarded in the first part of this study because of the presence of apatitic crystalline phases different from HAp, inspection of the SEM micrographs (Figure 6e, left) obtained for s2 shows a different morphology than expected. Careful inspection of a high-magnification SEM image (Figure 6e, right) revealed the presence of sharp rods agglomerated in flake-like groups, which in turn forms elongated crystals with wider bases, resembling needles. Their sizes suggest that during the growth by agglomeration, the shape of the crystals can change. This fact has been attributed to the high pKa of methanol, which favors edge shaped morphologies.

In spite of the predominant crystalline phase is not HAp, s15 (500 mM, pH 9.9) shows different micrometric rods and plates filled with belts (Figure 7a). Plates and rods, which are in the micrometric-length scale (Table 3), were analyzed by means of Raman spectroscopy. Results revealed the predominant presence of HAp crystalline phase with a predominant peak at 962 cm^{-1} for rods (Figure 7b), whereas the content of HAp phase is drastically reduced in front of other apatite phases (DCPD, β-TCP and ACP) for plates (Figure 7c). This result not only supports the fact that during agglomeration the final shape of the crystals can be tuned, but also expands the effect of pH to the control of micro-sized HAp rods with incredibly hexagonal shape.
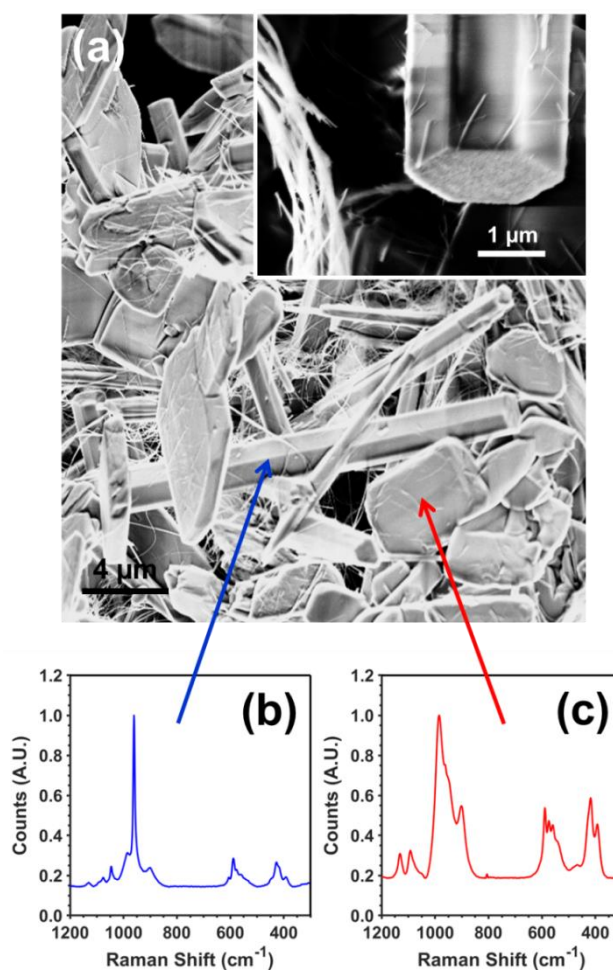
Figure 7. Effect of the composition on the morphology of the samples. (a) SEM micrograph displaying the rods, plates and belts obtained for sample s15. The inset shows a high magnification SEM micrograph of the hexagonal HAp rod. Raman spectrum recorded for (b) the hexagonal rod and (c) the plate, which the predominant presence of HAp and other apatatic phases, respectively.

CONCLUSIONS

Synthesis of pure and highly crystalline HAp with controlled size and shape can be achieved following a HT route without any additive using organic solvent and by controlling the pH and concentration conditions. Neutral or acidic pH increases the anisotropy of the growth. However, the lack of OH^- groups causes distortions and vacancies in the crystal lattice which are occupied by other species like HPO_4^{2-} or carbonate groups. In order to avoid this substitution, the utilization of non-aqueous

solutions as Ca^{2+} source allow working at alkaline pH without increasing the OH^- ion concentration, which is responsible of inhibiting the anisotropic growth. Ethanol has proven to be the optimum solvent, as it allows the control of crystals morphology (polymorphs spherical, rods, and belts) through pH and their sizes through ion concentration. The use of different solvents and pH control also affects the agglomeration step after the nucleation growth, leading to the formation of needle flake-like crystals (using methanol) and micrometric rods (using pH= 9.9). In summary, the method reported in this work allows to produce pure and crystalline HAp with controlled shape and size in a reproducible way using only organic solvent and controlling the pH.

ACKNOWLEDGEMENTS

SUPPORTING INFORMATION

The Supporting Information is available free of charge on the ACS Publications website at DOI:XXXXX. Description of the materials and characterization methods, FTIR and Raman spectra, and WAXS diffractograms.

REFERENCES

(1)   Li, Y. L.; Wang, Y. Q.; Li, Y. M.; Luo, W.; Jiang, J.; Zhao, J. Z.; Liu, C. S. Controllable Synthesis of Biomimetic Hydroxyapatite Nanorods with High Osteogenic Bioactivity. *ACS Biomater. Sci. Eng.* **2020**, *6*, 320–328.

(2)   Doustkhah, E.; Zare, R. N.; Yamauchi, Y.; Kafrani, T.; Mohtasham, H.; Esmat, M.; Ide, Y.; Fukata, N.; Rostamnia, S.; Sadeghi, M. H.; Assadi, M. H. N. Template-Oriented Synthesis of Hydroxyapatite Nanoplates for 3D Bone Printing. *J. Mater. Chem. B* **2019**, *7*, 7228–7234.

(3)   Chen, S.; Krumova, M.; Colfen, H.; Sturm, E. V. Synthesis of Fiber-like Monetite without Organic Additives and Its Transformation to Hydroxyapatite. *Chem. Mater.* **2019**, *31*, 1543–1551.

(4)   Ronan, K.; Kannan, M. B. Novel Sustainable Route for Synthesis of Hydroxyapatite Biomaterial from Biowastes. *ACS Sustain. Chem. Eng.* **2017**, *5*, 2337–2245.

(5)   Haider, A.; Haider, S.; Han, S. S.; Kang, I. K. Recent Advances in the Synthesis, Functionalization and Biomedical Applications of Hydroxyapatite: A Review. *RSC Adv.* **2017**, *7*, 7442–7458.

(6)   Sadat-Shojai, M.; Khorasani, M. T.; Dinpanah-Khoshdargi, E.; Jamshidi, A. Synthesis Methods for Nanosized Hydroxyapatite with Diverse Structures. *Acta Biomater.* **2013**, *9*, 7591–7621.

(7)   Kai, M. I.; Young, R. A; Posner, A. S. Crystal Structure of Hydroxyapatite. *Nature* **1964**, *204*, 1050–1052.

(8)   Palmer, L. C.; Newcomb, C. J.; Kaltz, S. R.; Spoerke, E. D.; Stupp, S. I. Biomimetic Systems for Hydroxyapatite Mineralization Inspired by Bone and Enamel. *Chem. Rev.* **2008**, *108*, 4754–4783.

(9)   Fihri, A.; Len, C.; Varma, R. S.; Solhy, A. Hydroxyapatite : A Review of

Syntheses, Structure and Applications in Heterogeneous Catalysis Q. *Coord. Chem. Rev.* **2017**, *347*, 48–76.

(10) Sadat-shojai, M.; Atai, M.; Nodehi, A.; Nasiri, L. Hydroxyapatite Nanorods as Novel Fillers for Improving the Properties of Dental Adhesives : Synthesis and Application. *Dent. Mater.* **2010**, *26*, 471–482.

(11) Rivas, M.; del Valle, L. J.; Rodriguez-rivero, A. M.; Turon, P.; Puiggali, J.; Alemán, C.; Puiggalí, J.; Alemán, C. Controlled Release and Delivery Systems Loading of Antibiotic into Biocoated Hydroxyapatite Nanoparticles : Smart Antitumor Platforms with Regulated Release. *ACS Biomater. Sci. Eng.* **2018**, 4, 3234–3245.

(12) Rivas, M.; del Valle, L. J.; Turon, P.; Alemán, C.; Puiggalí, J. Sustainable Synthesis of Amino Acids by Catalytic Fixation of Molecular Dinitrogen and Carbon Dioxide. *Green Chem.* **2018**, *20*, 685–693.

(13) Bose, S.; Saha, S. K. Synthesis and Characterization of Hydroxyapatite Nanopowders by Emulsion Technique. *Chem. Mater.* **2003**, *15*, 4464–4469.

(14) Vallet-Regí, M.; González-Calbet, J. M. Calcium Phosphates as Substitution of Bone Tissues. *Prog. Solid State Chem.* **2004**, *32*, 1–31.

(15) Epple, S. V. D.; Epple, M. Biological and Medical Significance of Calcium Phosphates. *Angew. Chem. Int. Ed.* **2002**, *41*, 3213–3215.

(16) Cai, Y.; Liu, Y.; Yan, W.; Hu, Q.; Tao, J.; Zhang, M.; Shi, Z.; Tang, R. Role of Hydroxyapatite Nanoparticle Size in Bone Cell Proliferation. *J. Mater. Chem.* **2007**, *17*, 3780–3787.

(17) Del Valle, L. J.; Bertran, O.; Chaves, G.; Revilla-lópez, G.; Rivas, M.; Casas, M. T.; Casanovas, J.; Turon, P.; Alemán, C. DNA Adsorbed on Hydroxyapatite Surfaces. *J. Mater. Chem. B,* **2014**, *2*, 6953–6966.

(18) Yelten-Yilmaz, A.; Yilmaz, S. Wet Chemical Precipitation Synthesis of Hydroxyapatite (HA) Powders. *Ceram. Int.* **2018**, *44*, 9703–9710.

(19) Abdelaal, M. Y.; Mohamed, R. M. Novel Pd / TiO 2 Nanocomposite Prepared by Modified Sol – Gel Method for Photocatalytic Degradation of Methylene Blue Dye under Visible Light Irradiation. *J. Alloys Compd.* **2013**, *576*, 201–207.

(20) Ashok, M.; Kalkura, S. N.; Sundaram, N. M.; Arivuoli, D. Growth and Characterization of Hydroxyapatite Crystals by Hydrothermal Method. *J. Mater. Sci. Mater. Med.* **2007**, *18*, 895–898.

(21) Ignjatovic, N.; Suljovrujic, E.; Budinski-simendic, J.; Krakovsky, I.; Uskokovic, D. Evaluation of Hot-Pressed Hydroxyapatite / Poly-L-Lactide Composite Biomaterial Characteristics. *J. Biomed. Mater. Res.* **2004**, *71B*, 284–294.

(22) Ferraz, M. P.; Monteiro, F. J.; Manuel, C. M. Hydroxyapatite Nanoparticles : A Review of Preparation Methodologies. *J. Appl. Biomater.* **2004**, *2*, 74–80.

(23) Neira, S.; Guitia, Guitián, F.; Taniguchi, T.; Watanabe, T.; Yoshimura, M. Hydrothermal Synthesis of Hydroxyapatite Whiskers with Sharp Faceted Hexagonal Morphology. *J. Mater. Sci.* **2008**, *43*, 2171–2178.

(24) Campus, Z.; Boukos, N. Controlling the Formation of Hydroxyapatite Nanorods with Dendrimers. *J. Am. Ceram. Soc.,* **2011**, *94*, 2023–2029.

(25) Viswanath, B.; Ravishankar, N. Biomaterials Controlled Synthesis of Plate-Shaped Hydroxyapatite and Implications for the Morphology of the Apatite Phase in Bone. *Biomaterials* **2008**, *29*, 4855–4863.

(26) An, L.; Li, W.; Xu, Y.; Zeng, D.; Cheng, Y.; Wang, G. Controlled Additive-Free Hydrothermal Synthesis and Characterization of Uniform Hydroxyapatite Nanobelts. *Ceram. Int.* **2016**, *42*, 3104–3112.

(27) Sadat-shojai, M.; Khorasani, M.; Jamshidi, A. Hydrothermal Processing of

Hydroxyapatite Nanoparticles — A Taguchi Experimental Design Approach. *J. Cryst. Growth,* **2012**, *361*, 73–84.

(28) Zhang, H.; Darvell, B. W. Formation of Hydroxyapatite Whiskers by Hydrothermal Homogeneous Precipitation Using Acetamide. *J. Am. Ceram. Soc.*, **2011**, *94*, 2007-2013.

(29) Yoshimura, M.; Sujaridworakun, P.; Koh, F.; Fujiwara, T.; Pongkao, D.; Ahniyaz, A. Hydrothermal Conversion of Calcite Crystals to Hydroxyapatite. *Materials Science and Engineering C,* **2004**, *24*, 521–525.

(30) Chye, S.; Loo, J.; Eva Siew, Y.; Ho, S.; Yin Chiang Boey, F.; Ma, J. Synthesis and Hydrothermal Treatment of Nanostructured Hydroxyapatite of Controllable Sizes. *J. Mater. Sci.* **2008**, 19, 1389–1397.

(31) Lak, A.; Mazloumi, M.; Mohajerani, M.; Kajbafvala, A.; Zanganeh, S.; Arami, H; Sadrnezhaad, S.K. Self-Assembly of Dandelion-Like Hydroxyapatite Nanostructures Via Hydrothermal Method. *J. Am. Ceram. Soc.* **2008**, *91*, 3292–3297.

(32) Zhu, R.; Yu, R.; Yao, J.; Wang, D.; Ke, J. Morphology Control of Hydroxyapatite through Hydrothermal Process. *J. Alloys Compd.* **2008**, *457*, 555–559.

(33) Zuo, G.; Wei, X.; Sun, H.; Liu, S. Zong, P.; Zeng, X.; Shen, Y. Morphology Controlled Synthesis of Nano-Hydroxyapatite Using Polyethylene Glycol as a Template. *J. Alloys Compd.* **2017**, *692*, 693–697.

(34) Aminian, A.; Solati-hashjin, M.; Samadikuchaksaraei, A.; Bakhshi, F. Synthesis of Silicon-Substituted Hydroxyapatite by a Hydrothermal Method with Two Different Phosphorous Sources. *Cerm. Int.* **2011**, *37*, 1219–1229.

(35) Wang, A.; Yin, H.; Liu, D.; Wu, H.; Wada, Y.; Ren, M.; Xu, Y.; Jiang, T.; Cheng, X. Effects of Organic Modifiers on the Size-Controlled Synthesis of

Hydroxyapatite Nanorods. *Appl. Surf. Sci.* **2007**, *253*, 3311–3316.

(36) Wang, P.; Li, C.; Gong, H.; Jiang, X.; Wang, H.; Li, K. Effects of Synthesis Conditions on the Morphology of Hydroxyapatite Nanoparticles Produced by Wet Chemical Process. *Powder Technol.* **2010**, *203*, 315–321.

(37) Rodríguez-Lugo, V.; Karthik, T. V. K.; Mendoza-Anaya, D.; Rubio-Rosas, E.; Villaseñor Cerón, L. S.; Reyes-Valderrama, M. I.; Salinas-Rodríguez, E. Wet Chemical Synthesis of Nanocrystalline Hydroxyapatite Flakes: Effect of PH and Sintering Temperature on Structural and Morphological Properties. *R. Soc. Open Sci.* **2018**, *5*, 180962.

(38) Xi, X.; Pi, X.; Nie, Z.; Song, S.; Xu, X.; Zuo, T. Synthesis and Characterization of Ultrafine WC-Co by Freeze-Drying and Spark Plasma Sintering. *Int. J. Refract. Metals Hard Mater.* **2009**, *1*, 101–104.

(39) Kim, J.; Kim, S. H.; Kim, H. K.; Akaike, T.; Kim, S. C. Synthesis and Characterization of Hydroxyapatite Crystals: A Review Study on the Analytical Methods. *J. Biomed. Mater. Res.* **2002**, *62*, 600–612.

(40) Rivas, M.; del Valle, L. J.; Armelin, E.; Bertran, O.; Turon, P.; Puiggalí, J.; Alemán, C. Hydroxyapatite with Permanent Electrical Polarization: Preparation, Characterization, and Response against Inorganic Adsorbates. *ChemPhysChem* **2018,** 19, 1746–1755.

(41) Postigo, M. A.; Katz, M. Solubility and Thermodynamics of Carbon Dioxide in Aqueous Ethanol Solutions. *J. Solution Chem.* **1987**, *16*, 1015–1024.

(42) Décultot, M.; Ledoux, A.; Fournier-Salaün, M.-C.; Estel, L. Solubility of CO_2 in Methanol, Ethanol, 1,2-Propanediol and Glycerol from 283.15 K to 373.15 K and Up to 6.0 MPa. *J. Chem. Thermodyn.* **2019**, *138*, 67–77.

(43) De Aza, P. N.; Guitián, F.; Santos, C.; De Aza, S.; Cuscó, R.; Artús, L.

Vibrational Properties of Calcium Phosphate Compounds. 2. Comparison between Hydroxyapatite and β-Tricalcium Phosphate. *Chem. Mater.* **1997**, *9*, 916–922.

(44) Sans, J.; Llorca, J.; Sanz, V.; Puiggalí, J.; Turon, P.; Alemán, C. Electrically Polarized Hydroxyapatite: Influence of the Polarization Process on the Microstructure and Properties. *Langmuir* **2019**, *35*, 14782–14790.

(45) Iqbal, Z.; Tomaselli, V. P.; Fahrenfeld, O.; Möller, K. D.; Ruszala, F. A.; Kostiner, E. Polarized Raman Scattering and Low Frequency Infrared Study of Hydroxyapatite. *J. Phys. Chem. Solids* **1977**, *38*, 923–927.

(46) Devarajan, V.; Klee, W. E. A Potential Model for Fluorapatite. *Phys. Chem. Minerals*, **1981**, 7, 35–42.

(47) Landi, E.; Tampieri, A.; Celotti, G.; Sprio, S. Densification Behavior and Mechanisms of Synthetic Hydroxyapatite. *J. Eur. Ceram. Soc.* **2000**, *20*, 2377–2387.

(48) Gonzalez-McQuire, R.; Chane-Ching, J. Y.; Vignaud, E.; Lebugle, A.; Mann, S. Synthesis and Characterization of Amino Acid-Functionalized Hydroxyapatite Nanorods. *J. Mater. Chem.* **2004**, *14*, 2277–2281.

(49) Bertran, O.; del Valle, L. J.; Revilla-López, G.; Rivas, M.; Chaves, G.; Casas, M. T.; Casanovas, J.; Puiggalí, J.; Alemán, C. Synergistic Approach to Elucidate the Incorporation of Magnesium Ions into Hydroxyapatite. *Chem. Eur. J.* **2014**, *21*, 2537–2546.

For Table of Contents Use Only

Controlled Anisotropic Growth of Hydroxyapatite by Additive-Free Hydrothermal Synthesis

Jordi Sans, Vanesa Sanz, Jordi Puiggalí, Pau Turon,[*] and Carlos Alemán[*]
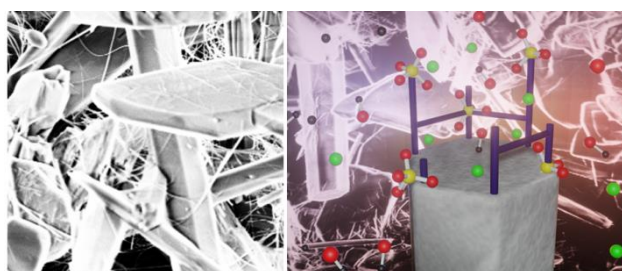
Synopsis: A new additive-free synthetic route, which is based on the hydrothermal method and the utilization of non-aqueous solvents, is proposed to control the morphology and crystallinity of hydroxyapatite.